

**The following resources related to this article are available online at [www.sciencemag.org](http://www.sciencemag.org) (this information is current as of December 3, 2009):**

**Updated information and services**, including high-resolution figures, can be found in the online version of this article at:

<http://www.sciencemag.org/cgi/content/full/317/5838/650>

**Supporting Online Material** can be found at:

<http://www.sciencemag.org/cgi/content/full/317/5838/650/DC1>

A list of selected additional articles on the Science Web sites **related to this article** can be found at:

<http://www.sciencemag.org/cgi/content/full/317/5838/650#related-content>

This article has been **cited by** 36 article(s) on the ISI Web of Science.

This article has been **cited by** 4 articles hosted by HighWire Press; see:

<http://www.sciencemag.org/cgi/content/full/317/5838/650#otherarticles>

This article appears in the following **subject collections**:

Materials Science

[http://www.sciencemag.org/cgi/collection/mat\\_sci](http://www.sciencemag.org/cgi/collection/mat_sci)

Information about obtaining **reprints** of this article or about obtaining **permission to reproduce this article** in whole or in part can be found at:

<http://www.sciencemag.org/about/permissions.dtl>

different core block chemistry. The key point for choosing the different chemistries of the two hydrophobic blocks is that the two blocks experience a high degree of mutual immiscibility. In the current experiment, polystyrene (PS) and poly(2,3,4,5,6-pentafluorostyrene) (PPFS) were employed as the different, third hydrophobic blocks in the two triblock copolymers (PAA<sub>94</sub>-*b*-PMA<sub>103</sub>-*b*-PS<sub>117</sub> and PAA<sub>93</sub>-*b*-PMA<sub>99</sub>-*b*-PPFS<sub>100</sub>) (29). Equal molar amounts of the two triblock copolymers with different respective third blocks were dissolved in pure THF. EDDA was then added to reach a final 1:1 molar ratio of amine groups to acid groups. The diamines underwent complexation with the PAA blocks, thereby forming aggregates with PAA-diamine cores. Notably, these aggregates contained each of the triblock copolymers with both PS and PPFS hydrophobic blocks because of the simple trapping of unlike hydrophobic blocks in the same aggregate by PAA-diamine complexation. Next, introduction of water into the THF solution to a final ratio of THF:water = 1:2 provided for the formation of cylindrical micelles. However, the existence of the original mixed triblock copolymer aggregates, as a result of PAA and diamine complexation, forced the local co-assembly of unlike third hydrophobic blocks into the same micelle core. In addition, the lack of chain exchange in solution that disallows global chain migration and maintains nonequilibrium micelle structures, combined with the fact that the PAA chains in the corona of the newly formed micelles were still complexed with diamines and were not freely mobile within the micelle, guarantee the stability of the mixed-core micelle. The immiscibility of the two different hydrophobic blocks, PS and PPFS, eventually resulted in internal phase separation on the nanoscale, producing multicompartment micelles. The images shown in Fig. 4, A to D were taken after 4 days of aging a solution of mixed hydrophobic core cylinders. Internal phase separation is clearly indicated by the strong undulations along the cylinder surfaces and the TEM contrast variation along the cylinders. The larger, darker, and more spherical regions within the cylinders are hypothesized to be regions that are concentrated in PAA<sub>94</sub>-*b*-PMA<sub>103</sub>-*b*-PPFS<sub>100</sub> triblock copolymer. First, there is a higher interfacial energy between PPFS and PMA, relative to PS and PMA, causing more chain stretching within PPFS-rich core domains so as to limit PPFS interactions with surrounding PMA blocks. Second, the greater electron density of the PPFS block provides a greater ability to scatter electrons and produce darker images in the TEM. The thinner region of the undulating cylinder would then be occupied primarily by PAA<sub>93</sub>-*b*-PMA<sub>99</sub>-*b*-PS<sub>117</sub> (Fig. 4G). This internal cylinder phase separation only occurred at relatively higher amounts of water in the mixed solvent solutions. Cryo-TEM showed uniform cylinders without undulation on the surface at only 40% water/THF solution after 4 days (Fig. 4E). However, multicompartment cylinders

could be observed as the water percentage increased to 67% (Fig. 4F). Reports in the literature have shown similar undulating cylinder morphologies through polymer blending, but with, at most, only three periods of undulation that always started from semispherical end caps (21). Clearly, the undulations shown here are not exclusively correlated with the spherical end caps and are obvious throughout the length of the cylinders. Safran *et al.* have demonstrated that the curvature energy of a cylinder with undulations could be lower than that of a nonundulating cylinder (31). However, the undulations observed here, although locally induced by unfavorable energetic interactions between PPFS and PS, are only possible kinetically because of the forced mixing of unlike hydrophobic core blocks as a result of PAA complexing with diamines and a specific solvent-mixing pathway.

Both the multicompartment cylinders with phase-separated cores and the cylindrical nanostructures with alternating layers of chemistry perpendicular to the cylinder axis are results of a solution assembly strategy to create structures with increased complexity with standard linear block copolymer architectures and chemistries. The key parameters are the combination of charged block interactions with multivalent counterions to influence both intra- and intermicellar interactions and solvent mixing to control the assembly pathways.

#### References and Notes

- Z. B. Li, E. Kesselman, Y. Talmon, M. A. Hillmyer, T. P. Lodge, *Science* **306**, 98 (2004).
- S. Jain, F. S. Bates, *Science* **300**, 460 (2003).
- B. M. Discher *et al.*, *Science* **284**, 1143 (1999).
- D. J. Pochan *et al.*, *Science* **306**, 94 (2004).
- J. Raetz, I. Manners, M. A. Winnik, *J. Am. Chem. Soc.* **124**, 10381 (2002).
- L. F. Zhang, A. Eisenberg, *Science* **268**, 1728 (1995).
- R. H. Zheng, G. J. Liu, X. H. Yan, *J. Am. Chem. Soc.* **127**, 15358 (2005).
- R. Zana, Y. Talmon, *Nature* **362**, 228 (1993).

- P. Ringle, G. E. Schulz, *Science* **302**, 106 (2003).
- P. W. K. Rothmund, *Nature* **440**, 297 (2006).
- C. A. Mirkin, R. L. Letsinger, R. C. Mucic, J. J. Storhoff, *Nature* **382**, 607 (1996).
- J. Cornelissen *et al.*, *Science* **293**, 676 (2001).
- J. P. Schneider *et al.*, *J. Am. Chem. Soc.* **124**, 15030 (2002).
- G. A. Silva *et al.*, *Science* **303**, 1352 (2004).
- A. P. Nowak *et al.*, *Nature* **417**, 424 (2002).
- W. U. Huynh, J. J. Dittmer, A. P. Alivisatos, *Science* **295**, 2425 (2002).
- L. Schmidt-Mende *et al.*, *Science* **293**, 1119 (2001).
- O. Kahn, C. J. Martinez, *Science* **279**, 44 (1998).
- M. Ouyang, D. D. Awschalom, *Science* **301**, 1074 (2003).
- V. Percec *et al.*, *Nature* **419**, 384 (2002).
- S. Jain, F. S. Bates, *Macromolecules* **37**, 1511 (2004).
- H. G. Cui, Z. Y. Chen, K. L. Woolley, D. J. Pochan, *Macromolecules* **39**, 6599 (2006).
- T. P. Lodge, *Macromol. Chem. Phys.* **204**, 265 (2003).
- R. Lund, L. Willner, D. Richter, E. E. Dormidontova, *Macromolecules* **39**, 4566 (2006).
- Y. Y. Won, H. T. Davis, F. S. Bates, *Macromolecules* **36**, 953 (2003).
- E. E. Dormidontova, *Macromolecules* **32**, 7630 (1999).
- Z. Y. Chen *et al.*, *J. Am. Chem. Soc.* **127**, 8592 (2005).
- Z. B. Li *et al.*, *Langmuir* **21**, 7533 (2005).
- Materials and methods are available as supporting material on Science Online.
- T. Tlusty, S. A. Safran, *Science* **290**, 1328 (2000).
- S. A. Safran, *Statistical Thermodynamics of Surfaces, Interfaces, and Membranes* (Addison-Wesley, New York, 1994).
- We thank NSF for funding, specifically the Nanoscale Interdisciplinary Research Teams program under grant DMR-0210247. Any opinions, findings, conclusions, or recommendations expressed in this material are those of the authors and do not necessarily reflect the views of NSF. We also thank the W. M. Keck College of Engineering electron microscopy laboratory at the University of Delaware and the nuclear magnetic resonance facilities of the Department of Chemistry at Washington University in Saint Louis.

#### Supporting Online Material

www.sciencemag.org/cgi/content/full/317/5838/647/DC1  
Materials and Methods  
Figs. S1 to S4  
Table S1  
References

26 February 2007; accepted 20 June 2007  
10.1126/science.1141768

## Capillary Wrinkling of Floating Thin Polymer Films

Jiangshui Huang,<sup>1,2</sup> Megan Juskiewicz,<sup>1</sup> Wim H. de Jeu,<sup>2,3</sup> Enrique Cerda,<sup>4</sup> Todd Emrick,<sup>2</sup> Narayanan Menon,<sup>1\*</sup> Thomas P. Russell<sup>2\*</sup>

A freely floating polymer film, tens of nanometers in thickness, wrinkles under the capillary force exerted by a drop of water placed on its surface. The wrinkling pattern is characterized by the number and length of the wrinkles. The dependence of the number of wrinkles on the elastic properties of the film and on the capillary force exerted by the drop confirms recent theoretical predictions on the selection of a pattern with a well-defined length scale in the wrinkling instability. We combined scaling relations that were developed for the length of the wrinkles with those for the number of wrinkles to construct a metrology for measuring the elasticity and thickness of ultrathin films that relies on no more than a dish of fluid and a low-magnification microscope. We validated this method on polymer films modified by plasticizer. The relaxation of the wrinkles affords a simple method to study the viscoelastic response of ultrathin films.

Thin sheets are much more easily bent than stretched by external forces. Even under purely planar tension, a sheet will often

deform out of plane to form wrinkles. This is an everyday phenomenon that can be seen on our skin as it is stretched by smiling, scars, or age;

on the film of cream that floats on warm milk; or on the skin of fruit as it dries.

This familiar instability occurs because the elastic energy required to stretch a sheet is reduced by the out-of-plane bending that accompanies wrinkling. Cerda and Mahadevan (1, 2) considered a situation in which a rectangular elastic sheet is clamped at its ends and stretched. Beyond a critical strain, the sheet wrinkles. Minimization of the total elastic energy leads to scaling relationships between the amplitude and wavelength of the wrinkles. Their arguments have been applied to a variety of contexts, including the mechanics of artificial skins (3, 4) and surgical scars (5).

We report on a study of wrinkling of films under capillary forces, which has thus far remained relatively unexplored. Because thin films are often immersed in fluid environments, both in biological and in synthetic soft materials, the elastic deformation of films under surface tension is relatively commonplace. Thin polymer films form an ideal experimental setting in which to explore wrinkling phenomena: We study films with very high aspect ratios (the ratio of diameter  $D$  to thickness  $h$  is  $D/h \sim 5 \times 10^5$ ), which can be treated accurately in the framework of two-dimensional elasticity.

We used films of polystyrene (PS; atactic, number-average molecular weight  $M_n = 91,000$ , weight-average molecular weight  $M_w = 95,500$ , radius of gyration  $R_g \sim 10$  nm) spin-coated onto glass substrates. The film thickness  $h$  was varied from 31 to 233 nm, as measured by x-ray reflectivity with a precision of  $\pm 0.5$  nm (6, 7). A circle of diameter  $D = 22.8$  mm was scribed onto the film with a sharp edge. When the substrate was dipped into a petri dish of distilled, deionized water, a circular piece of the PS film detached from the substrate. Because PS is hydrophobic, the film floated to the surface of the water where it was stretched flat by the surface tension  $\gamma$  of the air-water interface at its perimeter.

Wrinkles were induced in the stretched, floating film by placing a drop of water in the center of the film (Fig. 1), by placing a solid disk in the center of the film (fig. S1A), or by poking the film with a sharp point (fig. S1B) to produce a fixed out-of-plane displacement. All these methods of loading lead to qualitatively similar wrinkling patterns, radiating from the center of the load. We emphasize a crucial difference between loading with a solid and a fluid: The wrinkling induced in Fig. 1 is primarily due not to the weight of the drop, but to the capillary force

exerted on the film by the surface tension at the air-water-PS contact line. The radial stress  $\sigma_r$  induced at the edge of the drop is dominated by the surface tension, which for the conditions of Fig. 1 is about 100 times as great as the radial stress developed due to the weight of the drop ( $mg/2\pi a$ ), where  $m$  is the mass of the drop and  $a$  its radius. Indeed, a solid object of weight and contact area comparable to those of the drops shown in Fig. 1 would produce no discernible wrinkling. The contact angle of the drop on PS is  $88^\circ \pm 2^\circ$ , and thus the geometry of the drop on the film is approximately that of a hemisphere on a flat surface (with perhaps some deformation of the film close to the contact line itself). In view of this attractively simple geometry and the degree of experimental control afforded by loading with a fluid, we focus on wrinkling induced by fluid capillarity as in Fig. 1.

We observe the wrinkling pattern using a digital camera mounted on a low-magnification microscope (Fig. 1). Two obvious quantitative descriptors of the wrinkling patterns are the number of wrinkles  $N$  and the length of the wrinkle  $L$  as measured from the edge of the droplet.  $N$  is determined by counting. Because the terminus of the wrinkle is quite sharply defined and not

sensitive to lighting and optical contrast, we are also able to measure  $L$  directly from the image. The radius of the circle in which the entire wrinkle pattern is inscribed (see top left of Fig. 1) is determined with a precision of 3%.

The central question in understanding this wrinkling pattern is, how are  $(N, L)$  determined by the elasticity of the sheet (thickness  $h$ , Young's modulus  $E$ , and Poisson ratio  $\Lambda$ ) and the parameters of the loading (surface tension  $\gamma$  and radius of the drop  $a$ ). To study systematically the effect of loading and elasticity, we placed water drops at the center of the film using a micropipette, increasing the mass of the drop in increments of 0.2 mg. As the radius of the drop was increased, both  $L$  and  $N$  increased.

We first focus on  $N$ , which is found to increase as  $N \propto \sqrt{a}$ . However, as is evident in Fig. 1,  $N$  is smaller in thicker films. The combined dependence of  $N$  on  $a$  and  $h$  is correctly captured by the scaling  $N \sim a^{1/2}h^{-3/4}$ , as shown in Fig. 2. To understand this scaling, the arguments of Cerda and Mahadevan (2) may be adapted to a radial geometry (5, 8). Because the number of wrinkles remains constant at all radial distances  $r$  from the center of the pattern, the wavelength of wrinkles varies according to  $\lambda = 2\pi r/N$ .

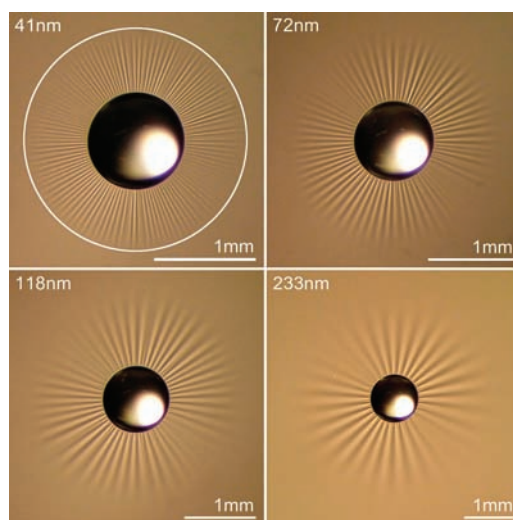


**Fig. 1.** Four PS films of diameter  $D = 22.8$  mm and of varying thicknesses floating on the surface of water, each wrinkled by water drops of radius  $a \approx 0.5$  mm and mass  $m \approx 0.2$  mg. As the film is made thicker, the number of wrinkles  $N$  decreases (there are 111, 68, 49, and 31 wrinkles in these images), and the length of wrinkles  $L$  increases.  $L$  is defined as shown at top left, measured from the edge of the water droplet to the white circle. The scale varies between images, whereas the water droplets are approximately the same size.

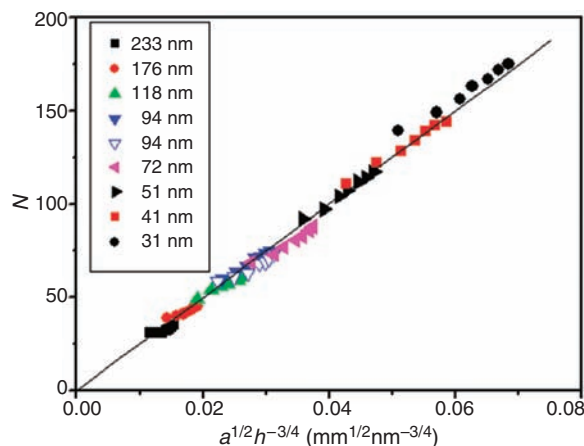


**Fig. 2.** The number of wrinkles  $N$  as a function of a scaling variable,  $a^{1/2}h^{-3/4}$ . Data for different film thicknesses  $h$  (indicated by symbols in the legend) collapse onto a single line (the solid line is a fit:  $N = 2.50 \times 10^3 a^{1/2}h^{-3/4}$ ). The extent of reproducibility is indicated by the open and solid inverted triangles, which are taken for two films of the same nominal thickness.

<sup>1</sup>Department of Physics, University of Massachusetts, Amherst, MA 31003, USA. <sup>2</sup>Polymer Science and Engineering Department, University of Massachusetts, Amherst, MA 31003, USA. <sup>3</sup>FOM Institute for Atomic and Molecular Physics, Amsterdam, Netherlands. <sup>4</sup>Departamento de Física, Universidad de Santiago de Chile, Santiago, Chile.

\*To whom correspondence should be addressed. E-mail: russell@pse.umass.edu (T.P.R.), menon@physics.umass.edu (N.M.)

**Fig. 3.** (A) Wrinkle length  $L$  is proportional to the drop radius  $a$ . For fixed loading,  $L$  increases with thickness  $h$ , as shown by the different symbols. (B) An approximate data collapse is achieved by plotting  $L$  against the variable  $ah^{1/2}$ . The inset at the top left shows the relation between  $L$  and  $h$  for a fixed radius of the water droplet  $a = 0.6$  mm. The black line is the best fit of the data to a power-law dependence:  $L = 0.0872 h^{0.58}$ ; the red line is the best fit to a square root:  $L = 0.129 h^{1/2}$ .

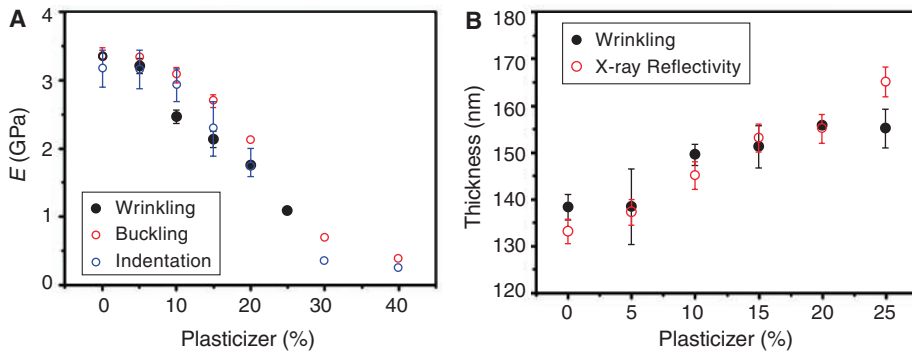
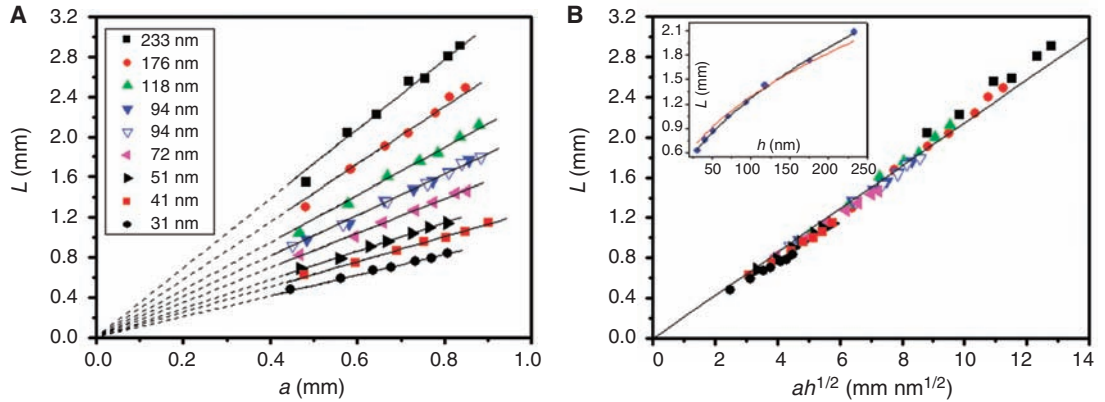


**Fig. 4.** (A) Young's modulus  $E$  versus concentration (by weight %) of plasticizer (dioctyl phthalate).  $E$  is computed from the wrinkling pattern (solid black symbols) by means of Eqs. 2 and 3. Data from other techniques (12) are shown for comparison. (B) Thickness  $h$  versus plasticizer concentration.  $h$  is computed from Eqs. 2 and 3; compare with data from x-ray reflectivity measurements (7). The error bars are the standard errors of the measurements.

This wavelength can be computed from a minimization of the bending transverse to the folds and the stretching along their length, which leads to

$$\lambda \sim (B/\sigma_{\pi})^{1/4} r^{1/2} \quad (1)$$

where the bending modulus  $B = Eh^3/12(1 - \Lambda^2)$  (9). For a circular film with a radial stress due to surface tension  $\gamma$  at the edge of the film and another surface tension  $\gamma$  at the boundary of the droplet,  $\sigma_{\pi} \sim \gamma a^2/r^2$  (10). We thus obtain

$$N = C_N \left[ \frac{12(1 - \Lambda^2)\gamma}{E} \right]^{1/4} a^{1/2} h^{-3/4} \quad (2)$$

where  $C_N$  is a numerical constant.  $C_N$  may be obtained from an analytical solution of the elastic problem or from an experiment like ours where all relevant parameters are known. Using literature values of  $E = 3.4$  GPa and  $\Lambda = 0.33$  for PS (11), and  $\gamma = 72 \pm 0.3$  mN/m, we obtain  $C_N = 3.62$  from the slope of the fit line in Fig. 2.

Before discussing wrinkle length, we make some qualitative remarks regarding the evolution of the wrinkle pattern. The wrinkles shown in the images are purely elastic deformations

and can be removed without the formation of irreversible, plastic creases (except possibly at the very center of the pattern). Despite this, the number of wrinkles in the pattern is hysteretic because there is an energy barrier as well as a global rearrangement involved in removing wrinkles. In Fig. 2, the drops are slowly increased in size by gentle addition of increments of water and thus represent our best experimental approximation to the equilibrium number of wrinkles. There is no measurable effect of contact line pinning. Nevertheless, the first droplet added invariably overshoots the equilibrium value of  $N$ , as may be seen in the slight curvature of individual sets of data in Fig. 2. The length of the ridge shows much less hysteresis because the length can locally increase or decrease continuously. This effect is clearly seen when the wrinkle pattern evolves as the drop is allowed to shrink by evaporation (fig. S2).

The length  $L$  of the wrinkle increased linearly with  $a$ , the radius of the drop, as shown in Fig. 3A. A simple argument for a linear increase was presented by Cerda (5), where the length of the wrinkle is dictated by the radial distance at which stress due to an out-of-plane force  $F$  applied at the center of a film decays to the value of the tension  $\tau$  applied at the distant boundaries.

This gives  $L \sim a(F/\tau)^{1/2}$ . In our situation  $F = 2\pi a\gamma$  and  $\tau = \gamma$ , thus yielding a linear dependence  $L \sim a$ . However, the data in Fig. 3A clearly show a dependence on thickness  $h$ , which is not captured by this argument. The dependence on  $a$  and  $h$  is reasonably well described by the purely empirical power-law scaling shown in Fig. 3B:  $L \sim ah^{1/2}$  (as shown in the inset to the figure, an unconstrained fit to a power-law yields a slightly better fit of  $L \sim ah^{0.58}$ ). This scaling is dimensionally incomplete and an additional factor of  $(\text{length})^{-1/2}$  needs to be taken into account. In terms of the available physical variables, the only possibility is  $(E/\gamma)^{1/2}$ , leading to

$$L = C_L \left( \frac{E}{\gamma} \right)^{1/2} ah^{1/2} \quad (3)$$

where  $C_L$  is a constant. From the fit shown in Fig. 3B, we obtain  $C_L = 0.031$ .  $E$  and  $h$  appear in Eq. 3 in the combination  $Eh$ , which is the stretching modulus of the sheet. This indicates that the length is defined purely by in-plane stresses. However, an attempt to write the radial stresses in a manner that is consistent with Eq. 3 yields an answer for  $\sigma_{\pi}(a)$  that is independent of surface tension, which is implausible. Thus, the dependence of  $L$  on  $h$  and  $a$  is adequately constrained by the experimental data and is well described by Eq. 3 but does not yet have a definitive explanation.

A measurement of  $N$  and  $L$  allows a determination of both  $E$  and  $h$  for a film, based on Eqs. 2 and 3. As a demonstration of this technique, we vary the elastic modulus of PS by adding to it varying amounts of di-octylphthalate, a plasticizer. As can be seen in Fig. 4A, we find good agreement with published data (12) obtained by other techniques. As a further test of our technique, we note that accompanying the large variation (greater than 300%) in Young's modulus, there is also a subtle change (of about 10%) in the thickness of the film as a function of the mass fraction,  $x$ , of plasticizer. The determination of thickness by means of Eqs. 2 and 3 yields a value that is in very close agreement

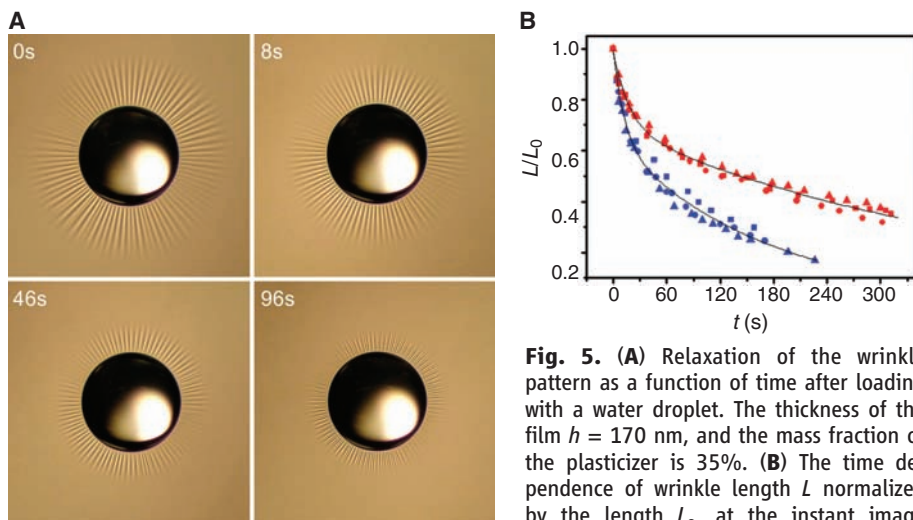


**Fig. 5.** (A) Relaxation of the wrinkle pattern as a function of time after loading with a water droplet. The thickness of the film  $h = 170$  nm, and the mass fraction of the plasticizer is 35%. (B) The time dependence of wrinkle length  $L$  normalized by the length  $L_0$ , at the instant image capture commenced. Data are shown for plasticizer mass fractions of 35% (blue symbols) and 32% (red symbols). The plot symbols differentiate experimental runs, showing reproducibility of the time dependence. Solid lines show fits to a stretched exponential:  $L(t)/L_0 = \exp[-(t/\tau)^\beta]$ .

(Fig. 4B) with our x-ray reflectivity measurements of  $h$ . Thus, measurements of both modulus and thickness can be achieved by a wrinkling assay with comparable or higher precision, and with very basic instrumentation, when compared to the other techniques on display in Fig. 4, each of which involves sophisticated equipment and yields only one of  $E$  or  $h$ .

Further, in contrast to the few other methods available for measuring the modulus of extremely thin films, such as nano-indentation (13) or stress-induced buckling (12), the measurement is performed with the film on a fluid surface, rather than mounted on a solid substrate. This allows the possibility for the film to relax internal mechanical stresses that can develop either in the spin-coating process or during transfer to a solid substrate. Apart from the ability to make measurements on a state that

is not pre-stressed, this opens the possibility of measuring bulk relaxational properties of the film without concerns about pinning to a substrate. In Fig. 5A, we show a sequence of images visualizing the time-dependent relaxation of the wrinkle pattern formed by a capillary load. At increasing time, the wrinkles smoothly reduce in length and finally disappear. The strains that develop in response to the capillary load (14) can relax due to the viscoelastic response of the PS charged with a large mass fraction of plasticizer. In Fig. 5B, we show the time dependence of wrinkle length,  $L(t)$ , for two sets of films with different plasticizer mass fraction,  $x$ .  $L(t)$  can be fit with a stretched exponential function  $L_0 \exp[-(t/\tau)^\beta]$ , where  $\tau$  decreases with increasing plasticizer concentration, and  $\beta = 0.50 \pm 0.02$ , typical of polymer viscoelastic response near the glass transition (13, 15).

Thus, capillary-driven wrinkle formation can be used as the basis for a metrology of both the elastic modulus and the thickness of ultrathin films by means of a very elementary apparatus—a low-magnification microscope and a dish of fluid. This simple technique can also be used to study dynamical relaxation phenomena in ultrathin films.

#### References and Notes

1. E. Cerda, K. Ravi-Chander, L. Mahadevan, *Nature* **419**, 579 (2002).
2. E. Cerda, L. Mahadevan, *Phys. Rev. Lett.* **90**, 074302 (2003).
3. K. Efimenko *et al.*, *Nat. Mater.* **4**, 293 (2005).
4. J. Genzer, J. Groenewold, *Soft Matter* **2**, 310 (2006).
5. E. Cerda, *J. Biomech.* **38**, 1598 (2005).
6. T. P. Russell, *Mat. Sci. Rep.* **5**, 171 (1990).
7. Supporting material is available on Science Online.
8. J.-C. Geminard, R. Bernal, F. Melo, *Eur. Phys. J. E* **15**, 117 (2004).
9. L. D. Landau, E. M. Lifshitz, *Theory of Elasticity, Course of Theoretical Physics* (Butterworth-Heinemann, India, ed. 3, 1986), vol. 7.
10. S. Timoshenko, J. Goodier, *Theory of Elasticity* (McGraw-Hill, New York, ed. 3, 1987).
11. J. Brandrup, E. H. Immergut, *Polymer Handbook* (Wiley, New York, ed. 3, 1989).
12. C. M. Stafford *et al.*, *Nat. Mater.* **3**, 545 (2004).
13. K. Miyake, N. Satomi, S. Sasaki, *Appl. Phys. Lett.* **89**, 031925 (2006).
14. H. Bodiguel, C. Fretigny, *Eur. Phys. J. E* **19**, 185 (2006).
15. N. G. McCrum, B. E. Read, G. Williams, *Anelastic and Dielectric Effects in Polymeric Solids* (Wiley, London, 1967).
16. We acknowledge support from the Center for University of Massachusetts–Industry Cooperative Research Program (J.H.); the NSF-supported Materials Research Science and Engineering Center on Polymers at the University of Massachusetts (W.H.J.); the U.S. Department of Energy, Office of Basic Energy Science, through DE-FG-0296 ER45612 (T.P.R.); and the NSF through contracts NSF-DMR 0606216 (N.M.) and NSF-CBET-0609107 (T.S.E., T.P.R., and N.M.). We gratefully acknowledge useful conversations with A. D. Dinsmore.

#### Supporting Online Material

www.sciencemag.org/cgi/content/full/317/5838/650/DC1  
Materials and Methods  
Figs. S1 and S2

3 May 2007; accepted 15 June 2007  
10.1126/science.1144616

## The Source of Saturn's G Ring

Matthew M. Hedman,<sup>1\*</sup> Joseph A. Burns,<sup>1,2</sup> Matthew S. Tiscareno,<sup>1</sup> Carolyn C. Porco,<sup>3</sup> Geraint H. Jones,<sup>4,5</sup> Elias Roussos,<sup>4</sup> Norbert Krupp,<sup>4</sup> Chris Paranicas,<sup>6</sup> Sascha Kempf<sup>7</sup>

The origin of Saturn's narrow G ring has been unclear. We show that it contains a bright arc located  $167,495.6 \pm 1.3$  km from Saturn's center. This longitudinally localized material is trapped in a 7:6 corotation eccentricity resonance with the satellite Mimas. The cameras aboard the Cassini spacecraft mainly observe small (1 to 10 micrometers) dust grains in this region, but a sharp decrease in the flux of energetic electrons measured near this arc requires that it also contain larger (centimeter- to meter-sized) bodies whose total mass is equivalent to that of a ~100-meter-wide ice-rich moonlet. Collisions into these bodies may generate dust, which subsequently drifts outward to populate the rest of the G ring. Thus, the entire G ring could be derived from an arc of debris held in a resonance with Mimas.

The G ring is unique among Saturn's major rings in that, before the arrival of the Cassini spacecraft, there was no obvious explanation for its location. The dust-sized particles that dominate this ring's optical properties should

erode quickly in Saturn's magnetosphere, yet there was no direct evidence for larger source bodies that could replenish the dust and no clear explanation for the concentration of such bodies in this one region (1–5). Unlike the E and F rings,

which are closely associated with satellites that could either directly supply material to the ring (Enceladus) or potentially confine the ring particles into a narrow region (Prometheus and Pandora), the G ring is located 168,000 km from Saturn's center, over 15,000 km from the nearest known satellite. However, using data from the remote-sensing and in situ instruments onboard

<sup>1</sup>Department of Astronomy, Cornell University, Ithaca, NY 14853, USA. <sup>2</sup>Department of Theoretical and Applied Mechanics, Cornell University, Ithaca, NY 14853, USA. <sup>3</sup>Cassini Imaging Central Laboratory for Operations, Space Science Institute, Boulder, CO 94043, USA. <sup>4</sup>Max Planck Institut für Sonnensystemforschung, Katlenburg-Lindau 37191, Germany. <sup>5</sup>Mullard Space Science Laboratory, Department of Space and Climate Physics, University College London, Holmbury St. Mary, Dorking, Surrey RH5 6NT, UK. <sup>6</sup>Applied Physics Laboratory, Johns Hopkins University, Laurel, MD 20723, USA. <sup>7</sup>Max Planck Institut für Kernphysik, Saupfercheckweg 1, 69117 Heidelberg, Germany.

\*To whom correspondence should be addressed. E-mail: mmhedman@astro.cornell.edu